Precursor of disintegration of Greenland's largest floating ice tongue

Angelika Humbert[1,2], Veit Helm[1], Niklas Neckel[1], Ole Zeising[1], Martin Rückamp[3,1], Shfaqat Abbas Khan[4], Erik Loebel[5], Dietmar Gross[6], Rabea Sondershaus[7], and Ralf Müller[7]

[1]Alfred-Wegener-Institut Helmholtz-Zentrum für Polar- und Meeresforschung, Bremerhaven, Germany
[2]University of Bremen, Department of Geosciences, Bremen, Germany
[3]Geodesy and Glaciology, Bavarian Academy of Sciences and Humanities, Munich, Germany
[4]DTU Space, National Space Institute, Technical University of Denmark, Department of Geodesy and Earth Observations, Copenhagen, Denmark
[5]Technische Universität Dresden, Institut für Planetare Geodäsie, Dresden, Germany
[6]Division of Solid Mechanics, Institute for Mechanics, Technical University of Darmstadt, Darmstadt, Germany
[7]Division of Continuum Mechanics, Institute for Mechanics, Technical University of Darmstadt, Darmstadt, Germany

Correspondence: Angelika Humbert (angelika.humbert@awi.de)

Abstract. The largest floating tongue of Greenland's ice sheet, Nioghalvfjerdsbræ, has so far been relatively stable with respect to areal retreat. Curiously, it experienced significant less thinning and ice flow acceleration than its neighbour Zacharias Isbræ. Draining more than 6% of the ice sheet, Nioghalvfjerdsbræ might become a large contributor to sea level rise in the future. Therefore, the stability of the floating tongue is a focus of this study. We employ a suite of observational methods to detect

5 recent changes. We found that the calving style has changed at the southern part of the eastern calving front from normal tongue-type calving to a crack evolution initiated at frontal ice rises reaching $5-7\,\mathrm{km}$ and progressing further upstream compared to 2010. The calving front area is further weakened by a substantial increase of a zone of fragments and open water at the tongue's southern margin, leading to the formation of a narrow ice bridge. These geometric and mechanical changes are a precursor of instability of the floating tongue. We complement our study by numerical ice flow simulations to estimate

10 the impact of future break-up or disintegration events on the ice discharge. These idealised scenarios reveal that a loss of the south-eastern area would lead to 1% of increase of ice discharge at the grounding line, while a sudden collapse of the frontal area (46% of the floating tongue area) will enhance the ice discharge by 8.3% due to loss in buttressing.

1 Introduction

15 The Greenland Ice Sheet (GrIS) has undergone major mass loss since the mid 1990's, with an acceleration of sea level contribution starting in the early 2000's (Shepherd et al., 2020) when outlet glaciers in the south accelerated and retreated (Joughin et al., 2004; Howat et al., 2008). Mass loss has reached northern Greenland since more than a decade with a significant contribution from ice dynamics beside the negative surface mass balance. (Khan et al., 2022). Only three floating glacier tongues are left to date (e.g. Hill et al., 2017), the other outlet glaciers became tidewater glaciers. The largest floating tongue in Greenland is

the Nioghalvfjerdsbræ (79°N Glacier, 79NG), draining an ice sheet area of 6.28% containing an ice volume of 0.58 m sea level
equivalent SLE (Krieger et al., 2020). Its ice front is still in contact with ice rises and it is hence an ideal object to understand
the transition from stability to disintegration.

Calving and basal melting are the predominant mass loss mechanisms of ice shelves and floating tongues. The style of
calving varies widely and is often governed by the existence of ice rises acting as pinning points. When the ice mass moves
passes by an ice rise, cracks are forming and generate rifts (cracks that are separating the ice entirely in vertical direction),
which grow laterally into the floating ice sheet. Eventually this leads to the detachment of an iceberg.

This calving style can be found at many locations and in the following we denote it as tongue-type calving. Tongue-type
calving is a normal process and is very distinct from break-up of disintegration events where ice shelves or floating tongues are
experiencing catastrophic fragmentation events. During these events, a large part is shattered and a massive number of icebergs
is produced in a short period of time (Braun et al., 2009). Prominent break-up events were observed for example at Larsen-B
(Rack and Rott, 2004), Wordie (Doake and Vaughan, 1991) and Wilkins (Humbert et al., 2010) ice shelves at the Antarctic
Peninsula.

In Greenland, the former floating tongue of Jakobshavn Isbræ has disintegrated in 2003 which led to acceleration of the
outlet glacier and increase in seasonality of glacier speeds (Joughin et al., 2012). The latest disintegration event in Greenland
has taken place at Zacharias Isbræ(ZI), which lost the majority of its floating tongue in the past decade. The glacier experienced
an ice flow acceleration and has turned into a tidewater glacier after this event (Mouginot et al., 2015). ZI and its neighbouring
glacier 79NG are the two major outlet glaciers of the Northeast Greenland Ice Stream (NEGIS), the only ice stream of the
GrIS.

The floating tongue of 79NG still exists. It has two calving fronts, one in the north towards the Djimphna Sound (earlier this
part of the 79NG was named Spalte Glacier) and one eastern calving front (see Fig. 1a) that is characterised by a number of
ice rises (blue areas in Fig. 1a) which act as pinning points. The latest calving event at the northern front was taking place in
2020, still in the same style as in the 1980's. Changes of calving front position and style in the past have not gone beyond the
line of these pinning points (Khan et al., 2014). A transition in calving regime can potentially destabilise the calving front and
eventually triggering the disintegration of the floating tongue.

Although large calving events are normal mass loss processes and are not considered as catastrophic events, the change in
load situation may lead to response in stresses of the inland ice glaciers. This has been shown in projections of the discharge of
Petermann Glacier for an upcoming calving event (Rückamp et al., 2019). Also for Pine Island Glacier a larger calving event
has been inferred to be a significant contribution to the ice flow acceleration since 2018 (Joughin et al., 2021), whereas ice flow
modelling showed that a moderate calving rate has a minor influence on the ice discharge across the grounding line (De Rydt
et al., 2021).

We leverage several satellite and airborne data to detect crack as well as calving front locations and to investigate changes of
the geometry of the floating tongue in the vicinity of the calving front. We mainly use optical, but also radar imagery, as well
as SAR interferometry and products such as velocity fields. Airborne data in this study comprises ice penetrating radar, laser
scanner (ALS) and optical imagery. The details of the data processing can be found in the Appendix A.
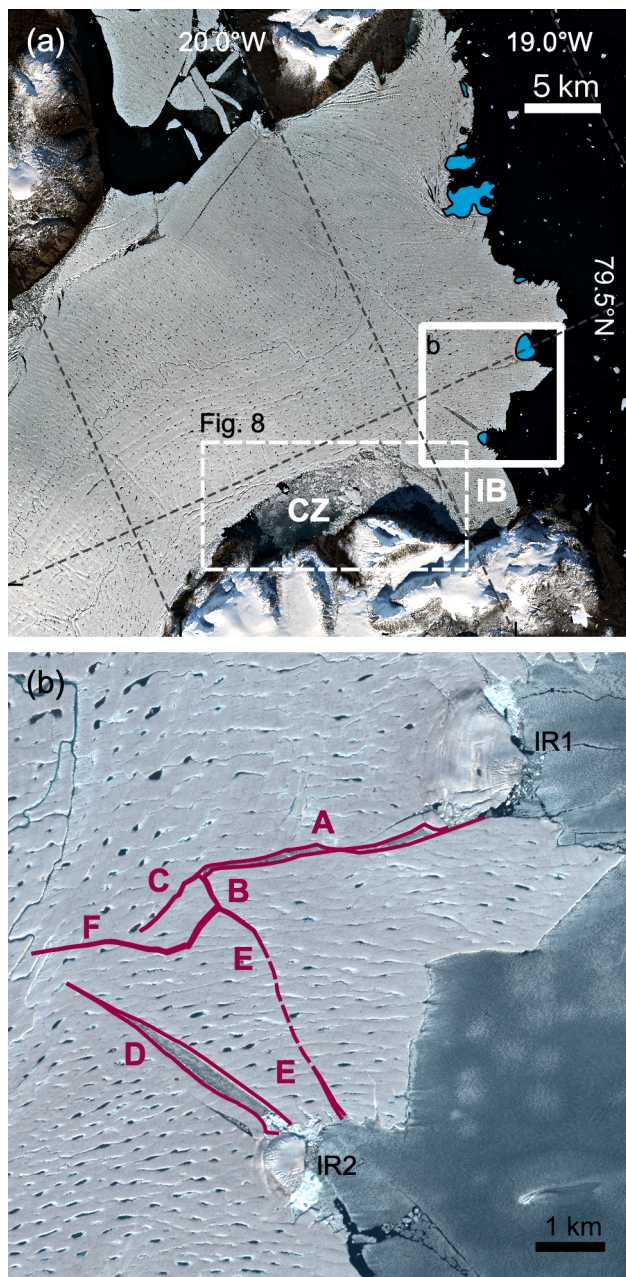
Figure 1. Overview of the eastern calving front of 79NG (background image Sentinel-2 2021-09-02). (a) Blue areas mark pinning points at the ice front. CZ indicates the southern chaos zone and IB marks an ice bridge (see text for details). The boxes indicate subsets used in (b) and in other figures. (b) Red lines denote cracks as by 2022-08-20 with names A-F mentioned in the main text. The naming is in alphabetic order starting with the oldest crack named A to the newest crack F.
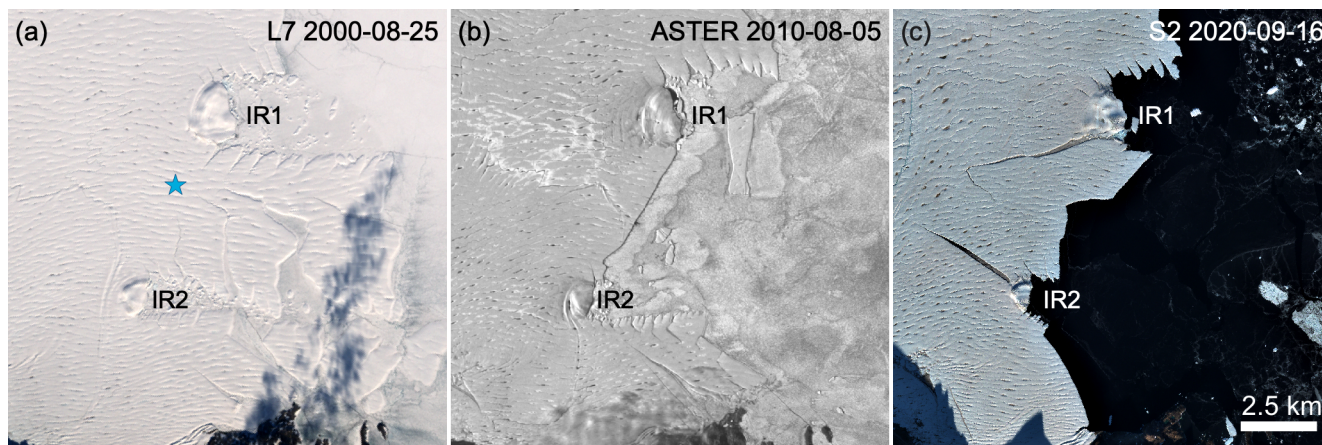
Figure 2. Evolution of the calving front and crack areas over two decades based on optical satellite imagery of (a) Landsat-7, (b) ASTER and (c) Sentinel-2 missions, respectively. The blue star denotes an area that has been partially grounded (see main text).

55   The observational datasets are complemented by numerous numerical modelling simulations (introduced in Appendix B). Based on this variety of datasets we aim to investigate whether recent changes of the 79NG configuration are indicating a regime change, what exactly is the cause of the changes and how this will impact the stability of 79NG.

The text is organised as follows: We first demonstrate that the calving style has changed, present a fracture mechanical assessment of the floating tongue at the calving front and discuss the evolution of a weak zone that potentially influences the
60   ice shelf stability. We continue with estimating the impact of future (large) calving events on 79NG's sea level contribution by means of ice flow modelling (details are presented in the Appendix B). Finally, we compare our findings with disintegration or catastrophic calving/disintegration events at other floating tongues and ice shelves.

2   Transition in calving regime

Comparing the calving front locations in optical satellite imagery allows to investigate whether the type of calving has changed.
65   Figure 2 displays the calving front in 2000, 2010 and 2020. While in 2000 (Fig. 2a) a tongue exists between the two ice rises and calving is initiated by the lateral rifts downstream of the ice rises, the calving front in 2020 (Fig. 2c) is characterised by rifts forming in upstream direction ranging more than $4\,\mathrm{km}$ (A and D in Fig. 1b).

Satellite imagery going back until 1975 shows that the tongue-type calving style has been present at least for 28 years until summer 2003. After 2003, the calving front retreated to a nearly straight line between the two ice rises (similar to Fig. 2b) and
70   remained in this shape until 2011. This is in line with the findings of (Khan et al., 2014). However, from mid 2010's onwards, the calving front situation has changed tremendously.
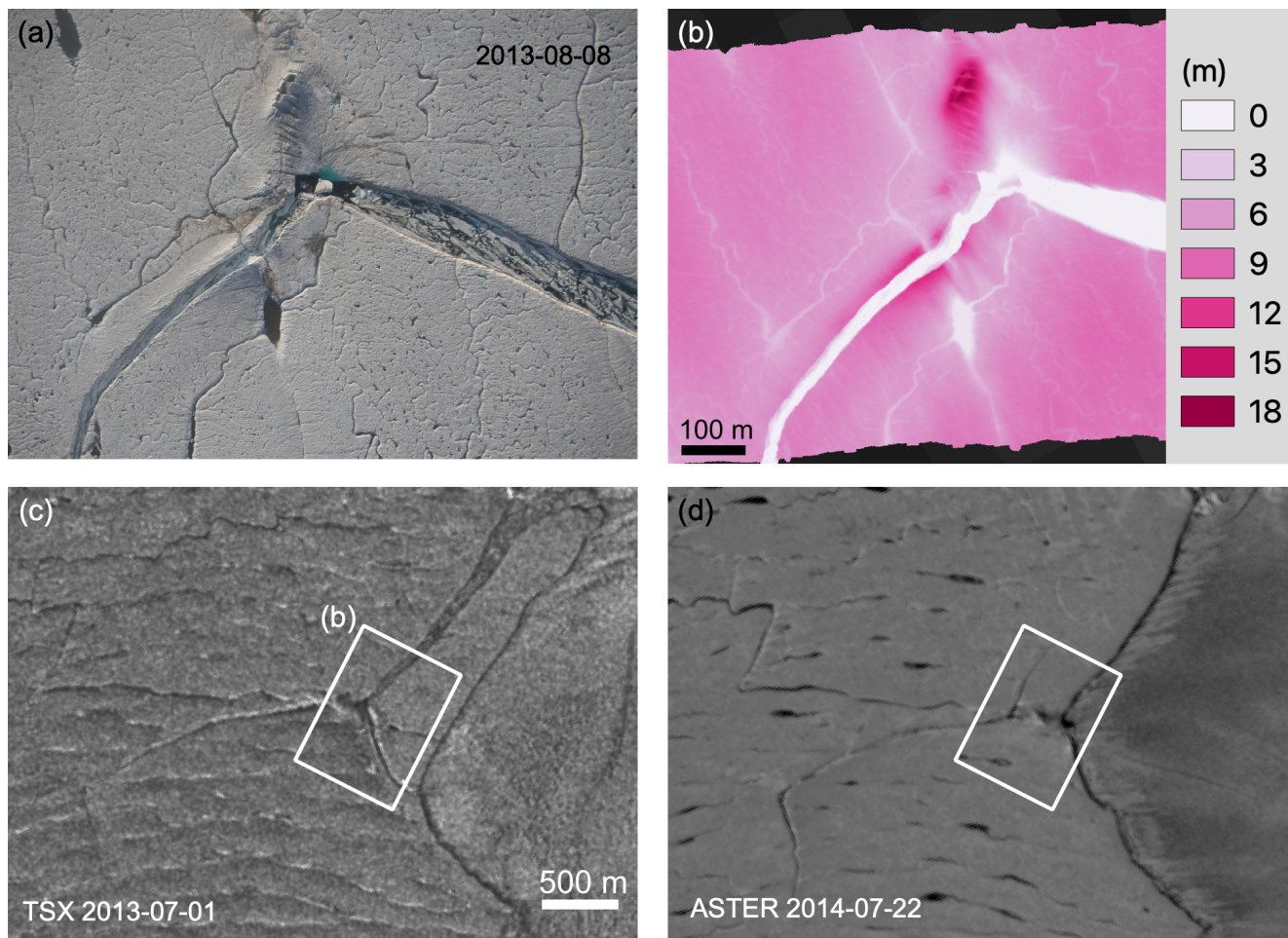
Figure 3. Former grounded spot. (a) photo of the Canon camera onboard Polar 5 crossing the grounded spot; (b) ALS surface elevation over at the same area as panel a; (c & d) satellite imagery during grounding (c) and after ungrounding (d). Panel d shows the area of panel b as an inset.

Figure 2a indicates that the lateral rifts are first growing towards the centre flowline between the ice rises, before changing orientation towards the spot marked with a blue star. This rift geometry, leading to tongue-type calving, is also found back to 1975 and icebergs until 2003 have been detached by these rifts, breaking L-shaped/wedge-shaped icebergs off.

75 Based on our database, we suggest that between the two ice rises a small grounded spot at location of the blue star (Fig. 2a) existed until 2013. That spot has become ungrounded early in 2014. Our assumption is based on the following observations: The surface structure as seen from the airborne optical camera on 08 August 2013 (Fig. 3a) is consistent with this spot being grounded as the surface elevation is $12\,\text{m}$ higher than the surrounding ice shelf (ALS in Fig. 3b) and the flow velocity is low (Fig. 6d). Evidence for ungrounding of this location comes from different data sources: satellite imagery showing this surface

80 buckle moving downstream (Fig. 3c,d) and ALS elevation data lacking the dome-like structure at the same location in 2021
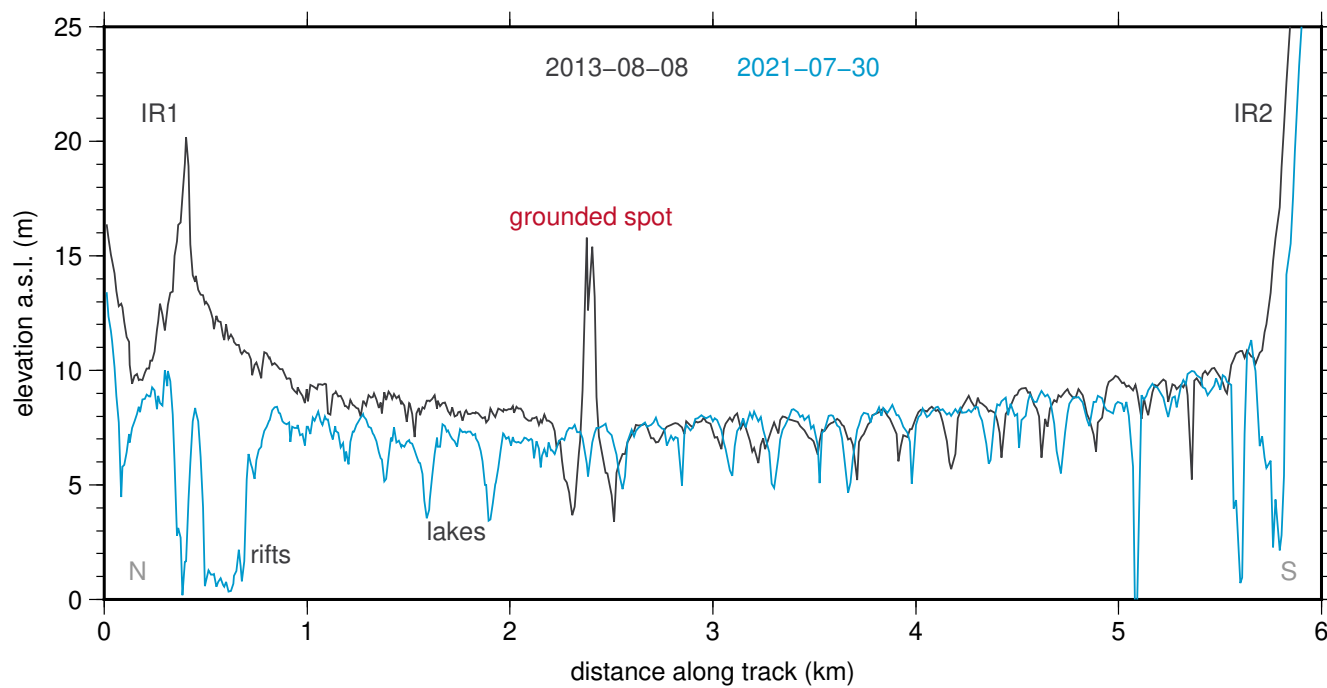
Figure 4. Thinning along the calving front between 2013 (grey line) and 2021 (blue line) based on ALS data. The location denoted with grounded spot corresponds to Fig. 3a. Elevations below $3\,\mathrm{m}$ belong to rifts in the vicinity of ice rise margins.

(Fig. 4). Since 2013 such dome-like structure was not newly formed, underlining this spot being in a transition to a new state. An alteration between grounding and ungrounding seems to be rather unlikely based on our data. To conclude, we infer that a former grounded spot existed which become afloat in the recent past.

Ungrounding can be a result from two instances: (i) thinner ice approaching the shallow bathymetry or (ii) thinning of the
85 ice locally. Repeat ALS elevation data from 2013 and 2021 reveal a difference of the ice surface of about $1.5\,\mathrm{m}$ north and almost no change south of that grounded spot (Fig. 4). We are aware that the surface elevation difference is only slightly above the tidal range, however, the thinning of the ice rises alone (left and right in Fig. 4) exemplifies that surface melting was taking place in these eight years.

Interestingly enough, ice penetrating radar (location of profiles shown in Fig. C2) shows in 2021 at the formerly grounded
90 spot still thinner ice (see Fig. 5). In 2013 the radargram clearly indicates reflection from a grounded spot, as presented in Fig. C1. This further supports the argumentation that this area was ungrounding.

Next to the ungrounding, we observe severe changes in the crack evolution at the calving front over the last years/decades. For the sake of clarity, we have denoted each crack with a label from A to F (Fig. 1b). Between 5–7 July 2016 crack A has been formed over a length of about $3\,\mathrm{km}$ and widened since. The shorter cracks B and C were formed two years later in June
95 2018. Crack D formed at the lower ice rise between 1–13 March 2019 ($3.5\,\mathrm{km}$ length). Both, crack A and D are actually rifts that intersect the ice entirely. The evolution of crack E is more difficult to obtain from satellite imagery: between May to
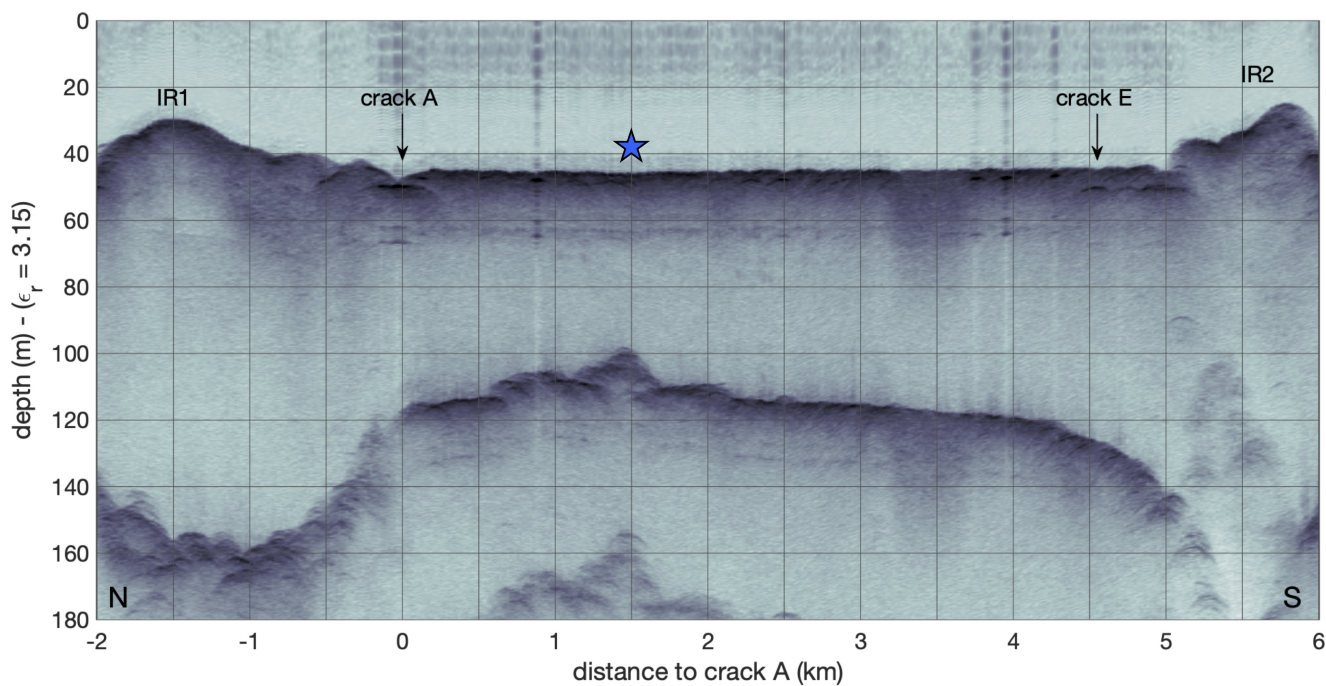
Figure 5. UWB echogram from 2021 showing crack A and E. The blue star marks the location of the grounded spot found in ALS surface elevation from 2013 (Fig. 4) and in EMR echogram (Fig. C1)

August 2019 it was formed in several episodes from two sides, starting from crack B and IR2. Although optical data show in 2021 nearly a unification (marked as dashed line in Fig. 1b and shown in high resolution in Fig. D2), there is no indication that they intersect the ice shelf entirely, which we discuss below in more detail. Crack F evolved in fall 2020 and has also

100   propagated slightly in winter 2021/22. Crack C has extended in early July 2022, while the crack at IR1 just north of crack A has propagated end of July 2022 towards the junction of crack A (visible in Fig. 1b). Most importantly, the crack evolution is reaching far upstream of the ice rises, marking the first event of this kind since the observational era at 79NG.

None of the cracks is a hydrofracture. Hydrofractures are basically crevasses filled with water, either from surface melt draining into them as on Antarctic ice shelves (e.g. Scambos et al., 2000) or are facilitating supraglacial lake drainage (e.g. Das

105   et al., 2008; Chudley et al., 2019). Although the floating tongue is densely covered with melt ponds in summer, we did not find evidence, that the melt ponds have an influence on the formation or propagation of the cracks.

The crack and rift evolution presented above is a complex process for which we develop next a fracture mechanical interpretation. We investigate the crack evolution and calving at 79NG's interesting part of the eastern calving front, unveil the modes under which the cracks are formed and discuss how that changed in the recent past. In fracture mechanics three distinct

110   crack modes are known: mode I is the tensile crack formation, mode II describes crack formation under in-plane shear and mode III the tear mode that acts out of plane. A tongue-type calving style is formed by ice rises inducing laterally dominant shear stresses that initiate mode II cracks (Fig. 2a). Once the ice moved past the ice rises, tensile stresses become large enough

for crack propagation as mode I cracks. The floating tongue downstream the ice rises is incised laterally on both sides and eventually one of those initial cracks become unstable and detaches an iceberg. This type of calving is still taking place north of 79.5°N (north of IR1, see Fig. 1, Fig. 2a and Khan et al. (2014)).

Figure 6 shows the first and second principal stresses between the ice rises with their corresponding directions calculated from a velocity field of 2014-16. Furthermore the figure displays the maximum shear stress and its direction. As pinning points are acting as barriers for the ice flow, their upstream side is characterised by compressive stresses. Consequently, shear zones exits between the compressive stress zone of each ice rise and the main flow between the two ice rises. The maximum shear stress descend towards zero in the main flow area.

The loss of the contact to the grounded spot is leading to an increase in the main flow, hence increase in horizontal shear stresses. This setting enabled the formation of mode II cracks, as crack A is one. Crack A runs into an area with low stresses (principal as well as shear stresses) and therefore stops propagating (see Fig. 6). Crack D is clearly a mode I crack and similar to what we found for crack A, it is arrested in an area of low principal stresses.

Interestingly enough, direction of crack propagation is neither along rivers or lakes nor along remnants of historic crevasses. We only find in the propagation of crack A one instance, where the running crack is joining for $\sim 200\,\mathrm{m}$ a river shore and deviates from it thereafter again. Crack arrest is not coinciding with rivers or lakes. In comparison with the ice thickness of about $80\,\mathrm{m}$ an $1-2\,\mathrm{m}$ deep river or $3-4\,\mathrm{m}$ (based on ALS data) deep lake is still a minor change in thickness.

The ice penetrating radar data from 2021 (overview of flight lines is presented in Fig. C2) across crack E revealed that the crack is not intersecting the ice entirely in vertical direction in end of July 2021 (Fig. 5, D1 and D2). However, surface imagery (Fig. D2) from the on-board camera in 2021, as well as optical satellite imagery (see Appendix A), show a thin surface crack at the same time (dashed line in Fig. 1b). In summer 2022, we find lakes ponding over this thin line and the surface ponds are not getting de-watered by crack E. Forming a non-intersecting crack is characteristic for a fatigue fracture. Fatigue fractures are initiated from cyclic loading situations on short time scales. The principal normal stresses between the ice rises are sufficiently low (Fig. 6a,b) to allow the existence and propagation of fatigue cracks. Here, tides are suggested to be the reason for the cyclic loading situation. To support this, we explore fringe patterns of interferograms from March 2021 (Fig. 7). Remarkably are clear hinge zones around IR1 and IR2, despite the fractures intersecting the ice vertically. We suggest that at IR2, the ice plate is pushed intensively against the ice rise, building a solid contact between the floating and grounded ice. At IR1, we suggest that there are still some intact connections between the floating part and the grounded ice of IR1. As a result, the deflection of the ice plate is a relative motion in vertical direction which leads to cyclic loading at crack E.

Currently the crack tip locations of the cracks D and F are located about $5-7\,\mathrm{km}$ further upstream than the calving front in 2010. Despite not yet being calved off, the rifts are already now intersecting the ice and as a consequence, the stresses in the floating tongue are changing.

We further consider potential future evolution at the calving front. We anticipate that calving along the cracks D–F–C–A detaching about $20\,\mathrm{km}^2$ of ice and a kind of ice bridge to remain (denoted IB in Fig. 1a; area $\sim 55\,\mathrm{km}^2$). This situation is comparable to the break-up event at Wilkins Ice Shelf (WIS), Antarctica, where a similar bridge was formed between stabilising islands (Braun et al., 2009). The WIS ice bridge had on one side a normal calving front, whereas the other side was supported

by a thick ice melange. In contrast, at 79NG the ice bridge has a calving front on both sides, one facing towards the open ocean to the east, another one towards a bay in the south. The southern calving front produces icebergs of smaller size that are trapped

150 in the bay, encaptured in winter by a seasonal melange, whereas in summer this melange opens up. We denote this area chaos zone (CZ in Fig. 1a) and investigate next the evolution of this zone, which we display in Fig. 8.

In 1990 this zone consisted of $14\,\mathrm{km}^2$ open area and further $17\,\mathrm{km}^2$ of fractured ice shelf. In 2000 the open area including icebergs was $21\,\mathrm{km}^2$ and about $19\,\mathrm{km}^2$ being fractured. This increased by August 2010 to $38\,\mathrm{km}^2$ and $16\,\mathrm{km}^2$ open and fractured areas respectively. In September 2020, the open area was $50\,\mathrm{km}^2$ with $15\,\mathrm{km}^2$ being fractured. The total area increased

155 by $34\,\mathrm{km}^2$ or 52% within 30 years, with $18\,\mathrm{km}^2$ increase in the same time as the calving style changed. Also the length of the calving front of this CZ has almost doubled with changing from $15\,\mathrm{km}^2$ to $28\,\mathrm{km}^2$.

The extent of the ice bridge in flow direction developed from 1996 $7.5\,\mathrm{km}^2$, 2013 and 2016 $5\,\mathrm{km}^2$ to $3.8\,\mathrm{km}^2$ in 2021, which is half the width in 25 years with 35% of loss in the past five years. For comparison, the ice bridge of Wilkins Ice Shelf had a width of $6\,\mathrm{km}^2$ prior to its rupture. However, an 'advantage' is here, that two smaller glaciers from Lambert Land are draining

160 into the ice bridge from south. This is leading to compression, which is visible in optical imagery and ALS elevation as bulging zone.
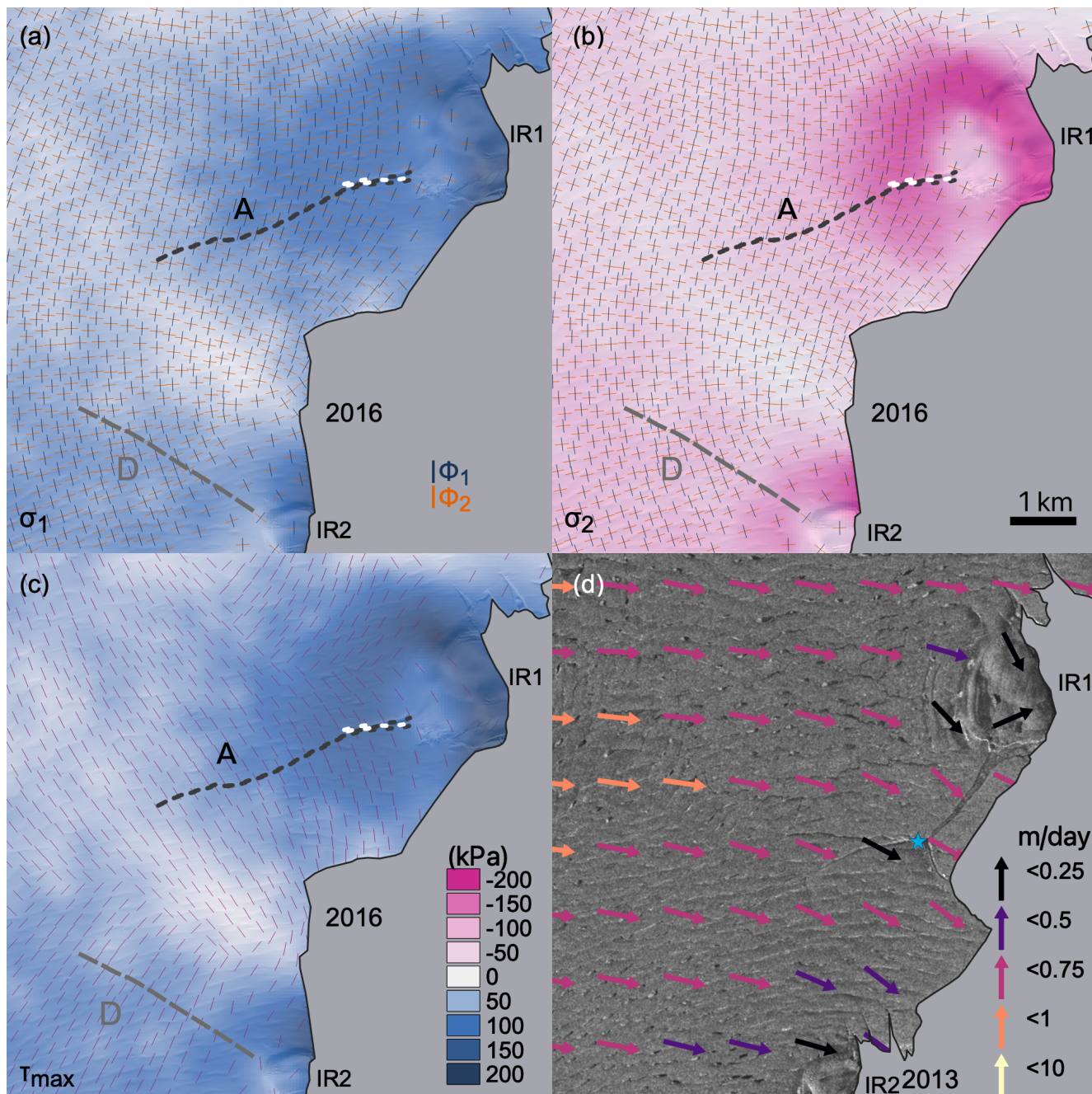
Figure 6. Principal stresses in 2016 and velocity field in 2013: (a) first principal normal stress, (b) second principal normal stress, at (a) and (b) crosses indicate principal stress directions (ϕ_1, ϕ_2) (c) maximum shear stress, lines indicate the direction (d) Velocity field in 2013 superimposed on a TerraSAR-X radar image. The blue star denotes the grounded spot. The white dashed line shows the initial crack A and the black one its length after the propagation in 2016. The grey dashed line represents crack D right after formation in 2019.
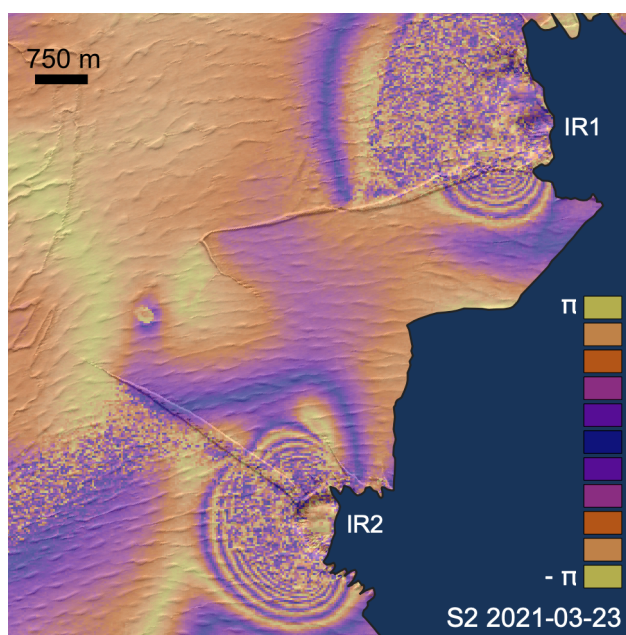
Figure 7. Double differential interferogram 2021-03-14, 2021-03-20 and 2021-03-26 based on Sentinel-1 and superimposed on a Sentinel-2 image of 2020-03-23.
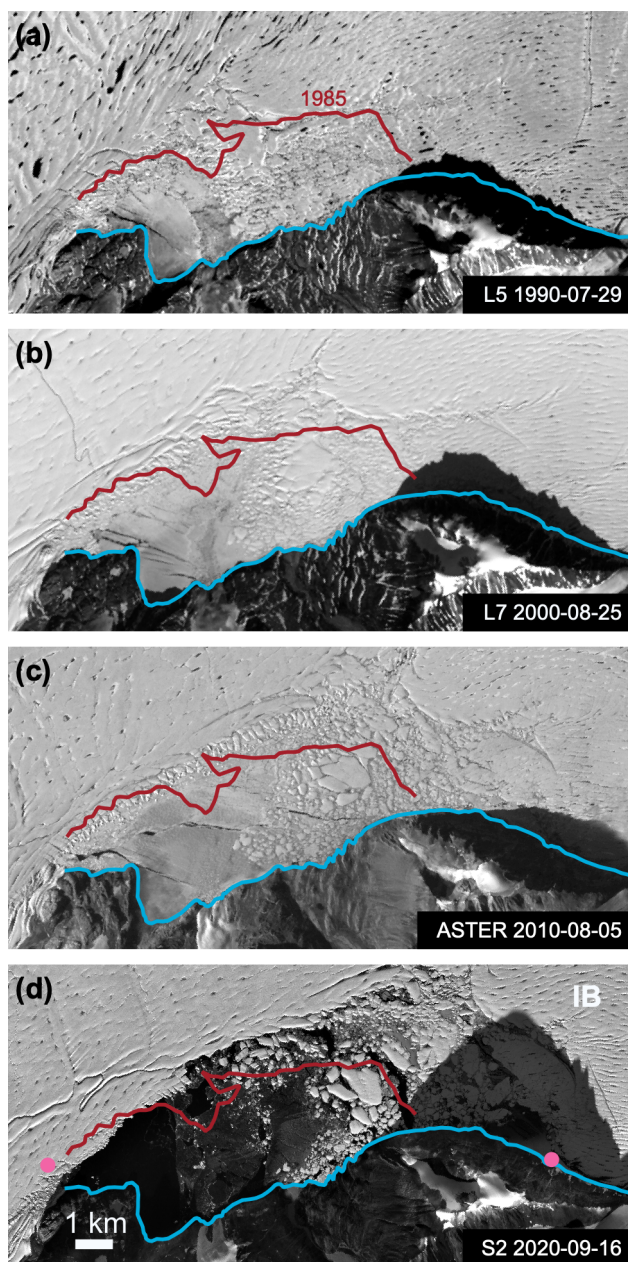
Figure 8. Evolution of the chaotic zone since 1990 in optical imagery (Landsat 5, 7, ASTER and Sentinel 2). The blue line marks the shore line. In panel (d), the pink dots mark an area without a hinge zone in interferograms.

3 Impact - response of 79NG instability of the calving front

Next we aim at constraining which impact the loss of parts of the 79NG's floating tongue will have on the ice discharge. As NEGIS is a fast flowing ice stream and drains a large area of the GrIS (17.23%, Krieger et al., 2020) it has the potential to
165 contribute to sea level rise by an increased ice discharge, once the boundary conditions, such as its calving front, are changing. We attempt to answer the question, how future large calving events or even a large disintegration event will modify the ice discharge. First, we initialise the model using observational data of surface and basal topography (Morlighem et al., 2017). We then use observed ice velocities (AWI-S1 velocities as in Krieger et al., 2020, but with Sentinel-1 winter (November-March) data from the years 2014 to 2016) as a target to determine the initial conditions by a running a joint inversion for the
170 basal friction coefficient and rigidity of the ice (see Appendix B). The initialisation experiment is denoted *init* and reveals a grounding line flux of $15.57\,\mathrm{Gt\,a^{-1}}$ (Fig. 9a). Subsequently, we perform two diagnostic perturbation experiments in which we remove sections of 79NGs ice tongue and assess the instantaneous glacier acceleration and increase in grounding line ice flux. The first experiment *calv-iceberg* retreats the calving front position in order to replicate a potential calving event following crack A towards the front of the chaos zone. The second experiment *calv2fjord* is investigating a more dramatic change in
175 the floating tongue, in which we assume that the calving front retreats until a slight bottleneck is reached (denoted southern and northern bottleneck (SBN and NBN), respectively, in Fig. 9g). This scenario mimics a sudden collapse of the frontal part, i.e. 46% of the floating tongue area. We then examine the instantaneous velocity change with respect to our initial modelled velocities and investigate changes in buttressing.

Up to the bottleneck (NBN to SBN in Fig. 9f) the ice shelf is currently nearly fully buttressed. Downstream of the bottleneck
180 a band of unbuttressed ice exists. The area around the eastern calving front is mainly overbuttressed as a result of the existence of the ice rises. With loss of the connection to the two southern ice rises (experiment *calv-iceberg*), only the northern tip of the calving front remains overbuttressed, while the central part of the ice shelf is remaining in similar state. This scenario shows a grounding line flux of $15.73\,\mathrm{Gt\,a^{-1}}$, which is an increase of 1%. With a further retreat (*calv2fjord*) the situation changes dramatically into an almost entirely underbuttressed ice shelf. This comes along with a speedup of the ice shelf and an increase
185 in ice discharge of 8.3% ($16.86\,\mathrm{Gt\,a^{-1}}$) compared to the *init* experiment.

4 Discussion

First we compare the situation at 79NG's eastern calving front with other ice shelves and floating tongues that have features similar to the ones at 79NG and have undergone considerable change in which these featured played a role. We start with WIS, that has been mentioned above already.
190 The ice bridge at WIS was much wider and also the confining islands had a larger size, leading to a broader contact with the confining margins. That ice bridge remained intact in its narrowest form for about 12 month, after which shattering of the ice bridge (Humbert et al., 2010) triggered a sequence of fast crack evolution before today's calving front settled. This can inform us about the time scale at which we shall expect events at 79NG's calving front to happen. Although 15% of area has been lost in only 14 months, a new, potentially intermediate, state has been reached that remained now for more than a decade.
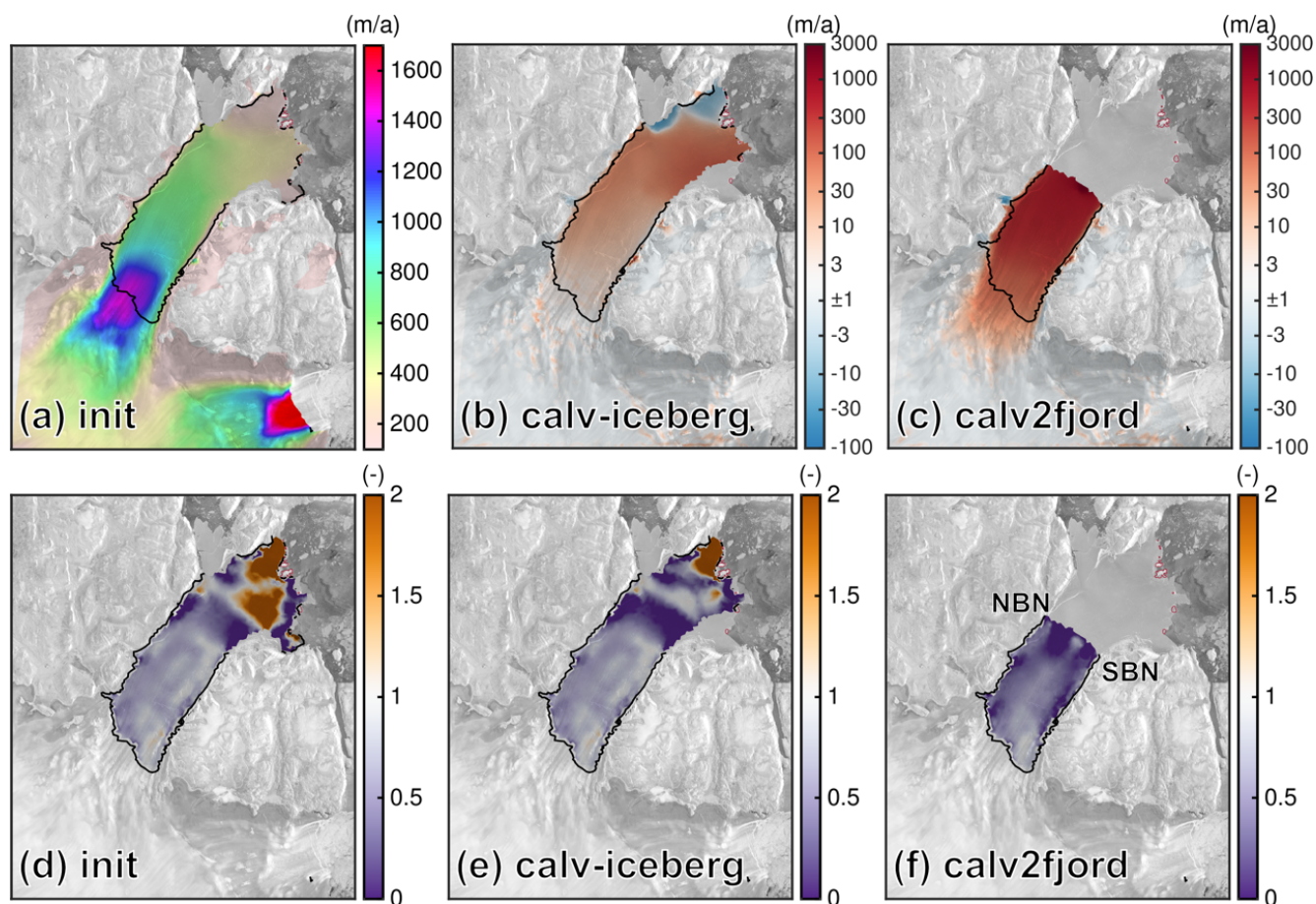
Figure 9. Simulation results of the ice flow model for the three experiments. Panel (a) shows simulated surface velocities for the *init* experiment. Panels (b) and (c) show velocity differences of the *calv-iceberg* and *calv2fjord* experiment to simulated velocities from the *init* experiment, respectively. Panels (d), (e), and (f) show the buttressing parameter according to Borstad et al. (2013). A value of 1 represent a fully buttressed ice shelf while a value of 0 an unbuttressed ice shelf. The black line indicates the grounding line from the *init* state. Panel f shows the locations of the northern and southern bottle neck (NBN) and (SBN), respectively.

195   Jakobshavn Isbrae (JI) has retreated past lateral embayment and we intend here to investigate if that situation is comparable to 79NG's chaos zone shown in Fig. 8. At JI the embayment had a length of about 12 km, with an ice rise being located at ∼ 5 km forming a shear margin between the fast glacier flow and the embayment with almost stagnant ice (Joughin et al., 2004). The retreat across this embayment from the ice rise upstream took place in less than 10 months. It is important to note, that the embayment was entirely filled with glacier ice, even with buckling along its margin, whereas at 79NG, the zone is

200   only filled with icebergs and seasonal sea ice, making it by far easier to retreat past this area. Comparing the retreat of the calving front of ZI with 79NG, it becomes evident, that most of the retreat of ZI appeared in a zone that has already been highly heterogeneous already in the 1980's. The northern part of 79NG's eastern calving front is somewhat similar to ZI's

north-eastern part, as both are stagnant and show similar surface buckling. In our simulations, this area is overbuttressed at 79NG (see Fig. 9), which one could argue too for ZI's northeastern part, which is still existing after the massive retreat of ZI's

205 calving front. In all three cases, WIS, JI and ZI, the events took place on short time scales, so only days to months after the disintegration has been triggered. This may partly been due to the fact that ice is a brittle material and fractures are propagating very fast (about a third of the speed of sound), but more prominent that ice is responding to change in stress state on short time scales elastically (e.g. Christmann et al., 2021). Once a change in the calving front situation occurs the elastic stress redistribute instantaneously and can trigger further follow up events as well as lead to a modified viscous response over month–years, see

210 Rankl et al. (2017) for WIS.

However, similar to the fact that WIS has not retreated further to date despite high number of annual melt days (Johnson et al., 2022) and JI's calving front retreat and acceleration has slowed down (Joughin et al., 2020), 79NG may retreat in episodes. However, the retreat to the bottleneck of the fjord (Fig. 9c,f) is already contributing significantly to sea level rise. Here, we did not consider any interactions with atmosphere and ocean, which will add to the changes in buttressing and acceleration.

215 The changes in air temperature across Greenland have recently been analysed by (Zhang et al., 2022). They present data from the weather station in Danmarkshavn, some $300\,\text{km}$ south of our study area, from 1958–2020, which shows a step in 2m-temperatures of more than one degree in the mid 1990's. This makes thinning of the floating tongue at the calving front more likely to arise from increased surface melting, than due to oceanic forcing. Schaffer et al. (2020) found warm water inflow into the cavity of 79NG at $400\,\text{m}$ depth and would thus not get in contact with the ice base at the calving front which consequently

220 also leads to low basal melt rates as shown by Wilson and Straneo (2015).

5 Conclusions

By means of remote sensing data, we detect changes of 79NG's eastern calving front that suggest the onset to destabilisation. Crack evolution is initiated at prominent ice rises and progressing far upstream. We identified crack initiation by shear mode, while crack propagation is in mode I and mode II for crack D and A, respectively. Interestingly, crack E is none of these but a

225 fatigue crack due to tidal forcing. As these crack patterns are very distinct from normal tongue-type calving we interpret the new crack formations as a precursor of disintegration. Moreover, we present evidence for ungrounding of a small pinning point due to thinning of the ice thickness after 2013. Basal melt rates are presumably small along the calving front, making thinning by surface melting a likely driver for this change. Not only at the eastern calving front changes are ongoing, but also at the southern margin of the floating tongue: in 2022 this margin has a calving front almost double as large as in 1985. The frontal

230 part of 79NG is thus weakened from both sides. An area of $\sim$5% of the floating tongue is likely to be lost in the near future. Numerical ice flow simulations show that already the loss of such relatively small area leads to an increase of the grounding line discharge of about 1% due to the reduction of the exerted buttressing. A sudden collapse of about 46% of the floating tongue further destabilises the glacier and will increase the ice discharge of 79NG's by 8.3%. Our findings indicate that 79NG is at the onset of a transition from stability to instability.

235 *Code and data availability.* The ice flow model ISSM is open source and freely available at https://issm.jpl.nasa.gov/ (Larour et al., 2012, last
access: August 25, 2022). Here ISSM version 4.19 is used. We provide the following data: laser scanner DEM of the region from 2013-08-08
and 2021-07-30, radargrams of the region from 2013-08-08 and 2021-07-30, optical imagery from the onboard camera from 2013-08-08
and 2021-07-30, simulated velocity and buttressing fields, principal strain-rates and principal directions for 2016 Ice flow velocities derived
from Landsat are available on the Geodetic data portal of TU Dresden (https://data1.geo.tu-dresden.de/flow_velocity, last access: August 25,
240 2022, Rosenau et al. (2015)).

Appendix A: Data

A1 Satellite data

For the analyses in this paper, we explore a range of different satellite sensors. Optical Landsat-5, -7 and -8, ASTER, as well as Sentinel-2 imagery is used to derive time series of calving front evolution. For this purpose, we use the radiometrically
245 calibrated and orthorectified Landsat Level-1 products provided by the United States Geological Survey and the Sentinel-2 Level-2A products provided by Copernicus, respectively.

Furthermore, we apply Landsat-8 imagery to determine ice flow velocity. This is realized through a combined feature tracking approach. We utilize the fast normalized cross correlation as well as a subsequent least squares matching in order to estimate displacement vectors with subpixel accuracy. A detailed description of the processing system is given by Rosenau et al. (2015).
250 Sentinel-1 synthetic-aperture radar (SAR) imagery is used for detecting calving front and crack positions. For this purpose, the data was first radiometrically calibrated and subsequently a Range-Doppler terrain correction was applied using the GIMP terrain model (Howat et al., 2014). We do not apply speckle filtering on purpose, in order to avoid smoothing of cracks. Mostly we use descending tracks with the relative orbit 170, which we found most useful for detecting crack evolution due to its orientation relative to the cracks.
255 With the availability of high resolution SAR data with frequent revisiting times, SAR interferometry (InSAR) became an important tool for monitoring the evolution of cracks on floating ice shelves (e.g. Rückamp et al., 2019; Libert et al., 2022). Here we applied SAR interferometry on Sentinel-1 Interferometric Wide (IW) data following Neckel et al. (2021). In a first step continuous single-look complex (SLC) images were generated from each set of bursts and swaths. SLC images of orbit 170, slice 2 were co-registered with the help of precise orbit information and the global TanDEM-X DEM gridded to 30 m
260 spatial resolution (Wessel et al., 2016). The accuracy of the co-registration was further refined by employing an iterative offset tracking approach between both SLCs. This is essential in fast flowing regions where phase jumps in burst overlap areas are most common. Two repeat-pass interferograms were generated with data acquired on 2021-03-14, 2021-03-20 and 2021-03-26. Topography induced phase information was removed from both interferograms employing the global TanDEM-X DEM. To minimize the effect of static horizontal ice flow a double differential interferogram was formed which is shown in Fig. 7.

265 A2 Ice penetrating radar

We used AWI's UltraWideBand (UWB) Multichannel Coherent Radar Depth Sounder (MCoRDS, version 5) onboard of the polar aircraft Polar 5 of the Alfred Wegener Institute Helmholtz Centre for Polar and Marine Research (AWI). The UWB has an array of eight antenna with a total transmit power of $6\,\mathrm{kW}$ and can be operated in the frequency band of $150 - 600\,\mathrm{MHz}$ (Hale et al., 2016). The radar was operated with a pulse repetition frequency of $10\,\mathrm{kHz}$ and a sampling frequency of $1.6\,\mathrm{GHz}$.
270 We used alternating sequences of different transmission/recording settings (waveforms) to increase the dynamic range: short pulses ($1\,\mu\mathrm{s}$) and low receiver gain ($11 - 13\,\mathrm{dB}$) to image the glacier surface, and longer pulses (3 and $10\,\mu\mathrm{s}$) with higher receiver gain ($48\,\mathrm{dB}$) to image internal features and the ice base. The waveforms were defined with regard to the thickness of the floating tongue. In our survey we used a bandwidth of $370\,\mathrm{MHz}$ within the frequency band of $150 - 520\,\mathrm{MHz}$. Post-flight

processing included pulse compression in range direction and synthetic aperture radar focusing in the along-track direction.

275 The final along track resolution was set to $10\,\mathrm{m}$. We assumed a relative permittivity of $\varepsilon_r = 3.15$ in ice for the time-to-depth conversion. The theoretical range resolution in ice after pulse-compression for the chosen bandwidth is about $0.23\,\mathrm{m}$. As there is no thick firn layer, we did not apply any firn correction. We concatenated the echograms of the alternating waveforms to obtain the final echograms covering the ice from the surface to the base with high dynamic range. Figure C2 gives an overview of the ice penetrating data used in this study.

A3 GNSS

The aircraft's position was measured using a dual-frequency NovAtel OEMV GNSS receiver at a sampling rate of $20\,\mathrm{Hz}$. To determine the flight trajectory we use the Precise Point Positioning (PPP) post processing option including precise clocks and ephemerides of the commercial GNSS software package Waypoint 8.90. The accuracy of the post processed trajectory is usually better than $0.1\,\mathrm{m}$ but varies along track.

A4 Laser scanner

Airborne laser scanner (ALS) data has been acquired in 2013 and 2021 with the laser scanner system (RIEGL LMS-VQ580) and a scan angle of $60°$. The aircraft was flying roughly $300\,\mathrm{m}$ above ground, resulting in a scan width of about $300\,\mathrm{m}$ and a mean point-to-point distance of $\sim 0.5\,\mathrm{m}$. To obtain the final calibrated geo-referenced point cloud (PC) data, the raw laser data was combined with the post-processed GNSS trajectory, corrected for altitude of the aircraft and calibration angles.

290 Crossovers were used to calibrate the system and to derive the elevation accuracy of the final geo-referenced PC to be better than $0.1 \pm 0.1\,\mathrm{m}$. The bias of $< 0.1\,\mathrm{m}$ varies along track and is due to the vertical accuracy of the post-processed GNSS trajectory. The final digital elevation model (DEM) with $1\,\mathrm{m}$ horizontal resolution was derived from the PC by using an inverse distance weighting (IDW) algorithm and a $5\,\mathrm{m}$ search radius. Finally, the freeboard was obtained by reducing the ALS DEM, that has been referenced to WGS84, to the EGM2008 geoid (Pavlis et al., 2012).

295 Please note that no tidal correction has been applied to the 2013 and 2021 DEM's. The tidal elevation is expected to be in the range of $1\,\mathrm{m}$ based on the measurements of Reeh et al. (2000), Christmann et al. (2021) and the FES2014b ocean tide model (Lyard et al., 2006) .

A5 RGB camera data

Next to the ALS data a nadir looking CANON EOS-1D Mark III Digital Single Lens Reflex (DSLR) camera in combination

300 with a CANON 14 mm f/2.8L II USM lens is routinely employed on board AWI's research aircrafts. RGB images are acquired at 6 second intervals and are stored together with a GNSS time tag in RAW data format. We selected all images acquired in the vicinity of the crack location and assigned the temporally closest dual-frequency GNSS and Inertial Navigation System (INS) measurement to each image. All images were then corrected for vignetting effects and converted into JPG format preserving the original high resolution. In the next step we employed the structure-from-motion pipeline of the commercial Agisoft Metashape

305   software (Beyer et al., 2018) to obtain a high resolution DEM and orthomosaic of the 2021 crack area. In order to match the orthomosaic with the timely consistent ALS DEM we coregister both DEMs and employed the derived translation and rotation information to transform the final orthomosaic image. The resulting mosais is displayed in Fig. D2.

Appendix B: ISSM model setup

The ice flow modelling of the NEGIS is conducted with the Ice-Sheet and Sea-level System Model (ISSM) (Larour et al.,
310   2012) and employs the Blatter-Pattyn approximation (Blatter, 1995; Pattyn, 2003). Model calculations are performed on an unstructured finite element grid with a horizontal resolution between 500 and 1000 m over fast flowing ice (Fig. B1). The domain is vertically extruded with 15 layers refined to the base.
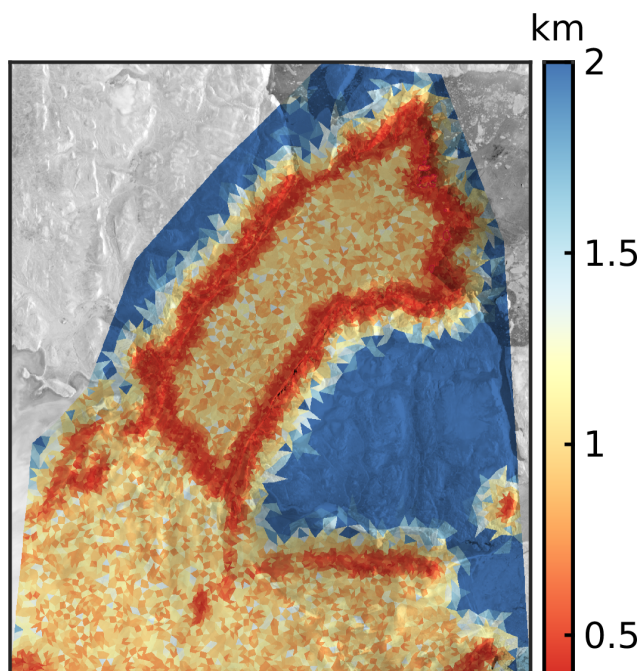
Figure B1. Horizontal mesh resolution (km). Data are clipped at 0.4 and 2 km. The horizontal resolution of a triangle is defined by its minimum edge length.

      We initialize the model using the present-day ice geometry from BedMachine Greenland version 4 (Morlighem et al., 2017). We reconstruct basal friction, k^2, and bulk ice rigidity, B, using data assimilation of satellite measurements of surface ice
315   velocity (Fig. B2) (AWI-S1 velocities as in Krieger et al., 2020, but with Sentinel-1 winter (November-March) data from the years 2014 to 2016). Since the surface velocity field have a different coverage as the BedMachine mask, we clipped the calving front to the coverage of the surface velocity field. We use a friction power law (Budd-like) on grounded ice that relates the

basal shear stress, $\boldsymbol{\tau}_b$, to the sliding velocity, $\boldsymbol{v}_b$,

$$\boldsymbol{\tau}_b = -N^{1/m} k^2 \left|\boldsymbol{v}_b\right|^{1/m-1} \boldsymbol{v}_b \tag{B1}$$

320   with the stress exponent $m = 3$. The effective pressure, N, is assumed to be the difference of ice overburden pressure, p_{i}, and the subglacial water pressure, p_{w}, i.e. $N = p_{\mathrm{i}} - p_{\mathrm{w}}$. The basal water pressure is computed in marine parts, i.e. where the ice base, z_{b}, is below the sea-level ($z_{\mathrm{b}} < z_{\mathrm{sl}}$), i.e. $p_{\mathrm{w}} = -\min(\varrho_{\mathrm{w}} g z_{\mathrm{b}}, 0)$, where $\varrho_{\mathrm{w}} = 1023\,\mathrm{kg\,m^{-3}}$ is the density of the ocean water.

The viscosity is given by the Glen-Steinemann flow law (Glen, 1955; Steinemann, 1954)

325   $$\eta = \frac{1}{2} B \dot{\varepsilon}_e^{(1-n)/n}, \tag{B2}$$

with the flow law exponent $n = 3$, the bulk ice rigidity B, and the effective strain rate $\dot{\varepsilon}_e$ being the second invariant of the strain-rate tensor.

To avoid having to invert for both bulk ice rigidity and basal friction at the same location, we apply an inversion of bulk ice rigidity to floating ice and basal friction to grounded ice only. We assume that the bulk ice rigidity is a constant value on
330   grounded ice equivalent to a temperature of -7°C.

Within the inverse problem a cost function, J, that measures the misfit between observed, $v_{x,y}^{\mathrm{obs}}$, and modelled velocities, $v_{x,y}$, is minimised. The cost function is composed of two terms which fit the velocities in fast- and slow-moving areas. A third term is a Tikhonov regularisation to avoid oscillations. The cost function is defined as follows:

$$J_0(\mathbf{v}) = +\gamma_1 \frac{1}{2} \int\limits_{d\Gamma_s} \ln\left(\frac{\sqrt{v_x^2 + v_y^2} + \varepsilon}{\sqrt{v_x^{\mathrm{obs}\,2} + v_y^{\mathrm{obs}\,2}} + \varepsilon}\right) d\Gamma_s, \tag{B3}$$

335   $$J_{\mathrm{reg}}(B \text{ or } k) = \gamma_t \frac{1}{2} \int\limits_{\Gamma_b} \nabla(B \text{ or } k) \cdot \nabla(B \text{ or } k)\, d\Gamma_b, \tag{B4}$$

$$J(\mathbf{v}, B \text{ or } k) = J_0(\mathbf{v}) + J_{\mathrm{reg}}(B \text{ or } k), \tag{B5}$$

where ε is a minimum velocity used to avoid singularities and Γ_s and Γ_b are the ice surface and ice base, respectively. An L-curve analysis was performed to pick the Tikhonov parameter γ_t. We obtained excellent agreement to the observed velocities by choosing $\gamma_1 = 1$ and $\gamma_t = 4 \times 10^{-9}$ (Fig. B3).
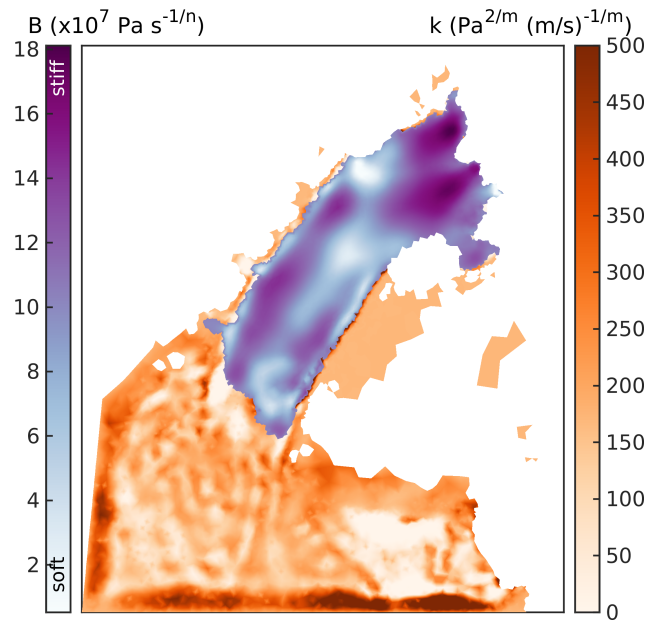
Figure B2. Inferred values for the basal friction coefficient k and the bulk ice rigidity B by the joint inversion.
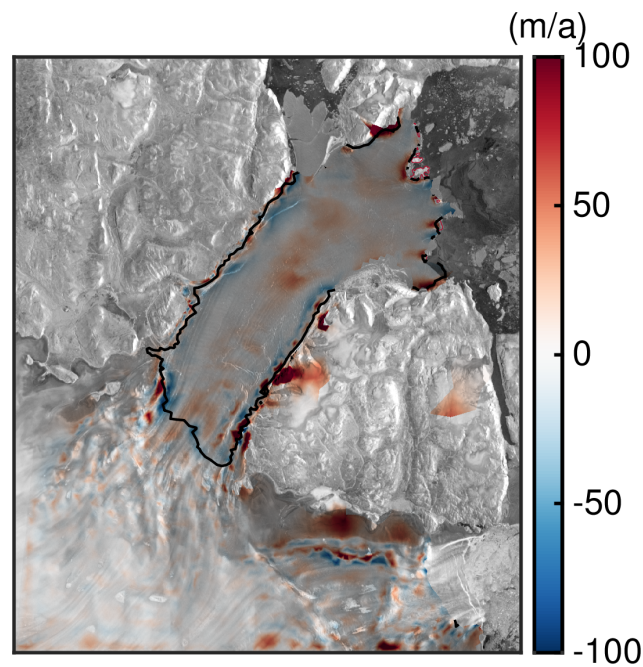
Figure B3. Surface velocity differences of simulated and observed velocities.

Appendix C: Ice penetrating radar

340
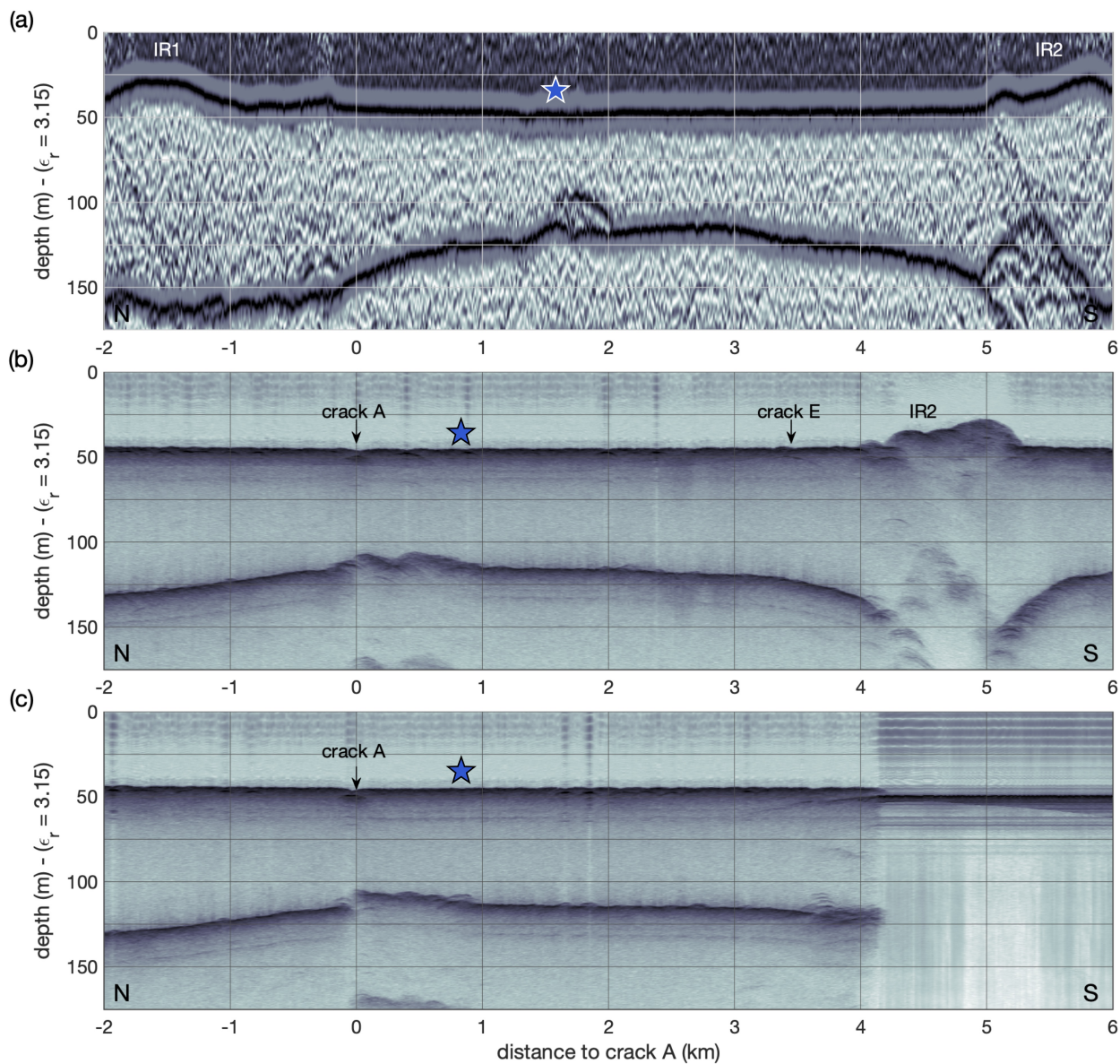
Figure C1. Airborne radar echograms recorded in study area and crossing today's crack A. (a) EMR echogram from 2013. (b,c) UWB echograms from 2021. The blue stars mark the location of the grounded spot found in (a) and in ALS elevation data from 2013 (Fig. 4).
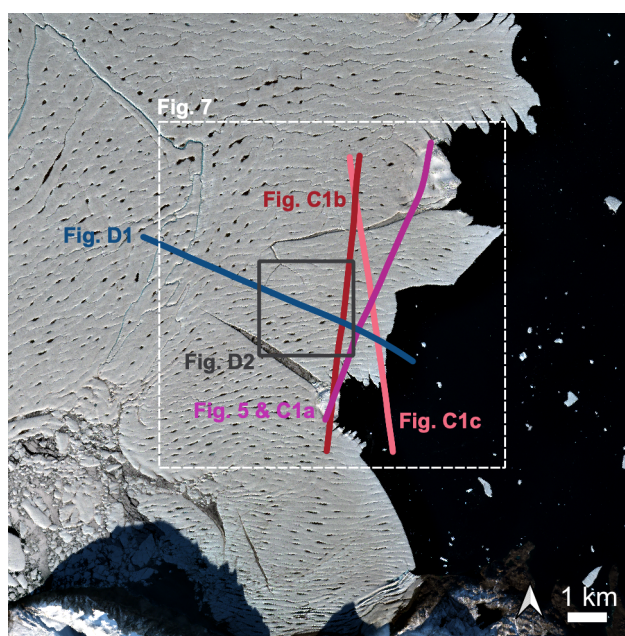
Figure C2. Overview of the UWB profiles displayed in Fig. 5, C1 (in redish color), the profile crossing crack E Fig. D1 (blue) and the area shown in Fig. 7 (white) and Fig. D2 (gray). The blue star denotes the location of the formerly grounded spot. The background image is a Sentinel-2 image from 2021-09-02.

Appendix D: Crack E
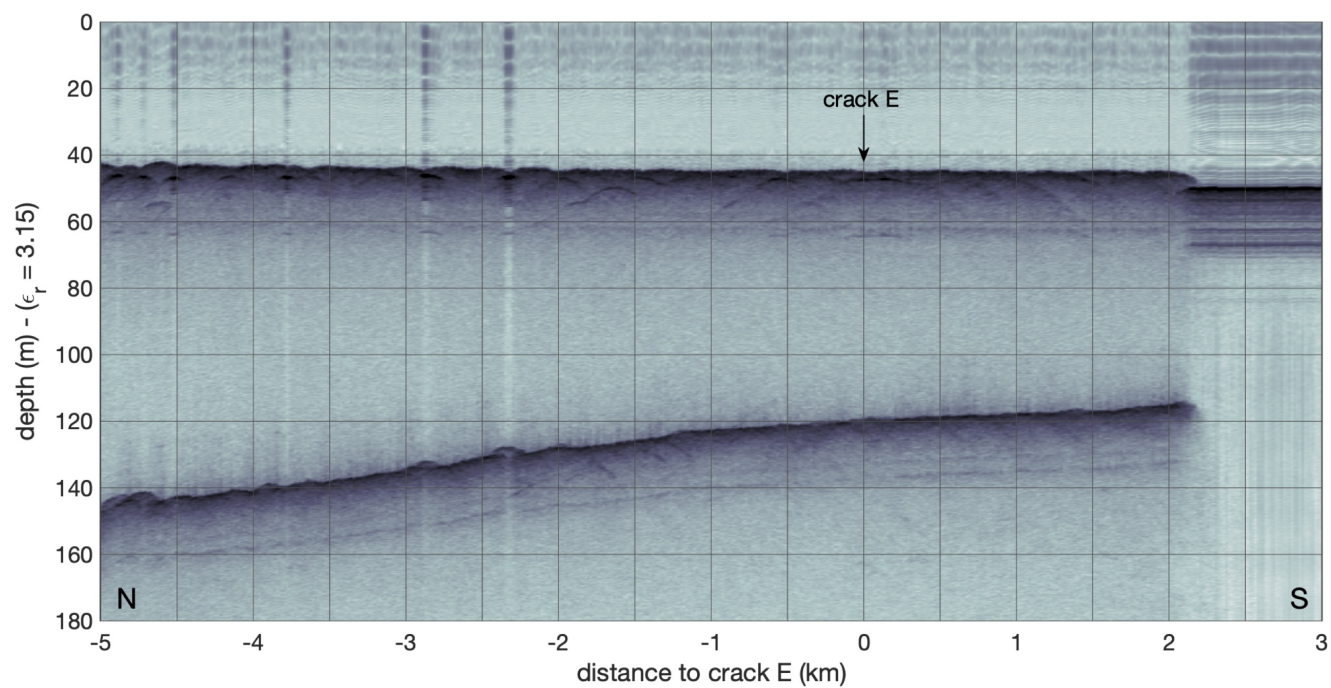
Figure D1. UWB echogram from 2021 crossing crack E. For orientation: flight direction is towards the calving front, that is located at 2 km distance from crack E.
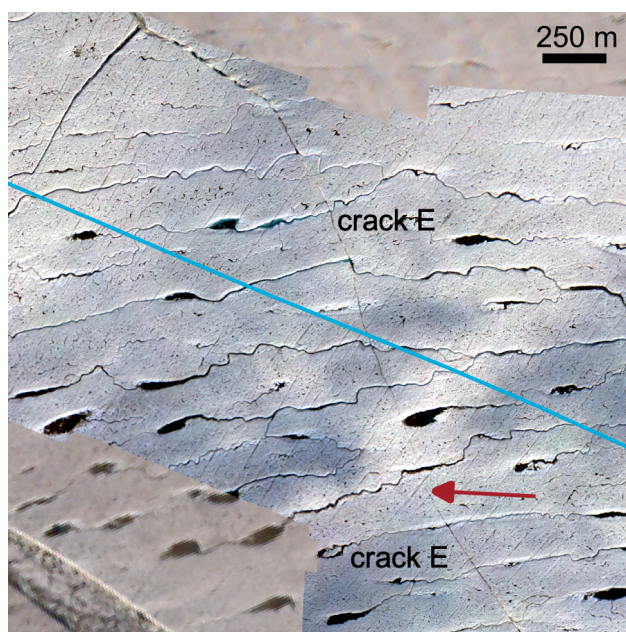
Figure D2. Mosaic of the onboard optical camera from a flight on 2021-07-30 superimposed on a Sentinel-2 image of the same date. The red arrow points to the location at which the cracks propagating from north and south will join. The flight track from Fig. D1 is shown as blue line. Note that the rivers and lakes through which the narrow crack E has propagated are not de-watered, pointing out that the crack is not extending through the entire ice thickness.

Author contributions. A.H. designed the study, processed and analysed the optical satellite data, M.R. conducted the ISSM simulations, D.G., R.M., R.S., A.H. conducted the fracture mechanical analysis, E.L. contributed satellite remote sensing velocity fields, N.N. computed interferograms and mosaiced the optical airborne imagery, V.H. processed the airborne laser scanner data, O.Z. and V.H. processed the
345 airborne ice penetrating data, S.A.K. contributed findings from his previous studies. All authors discussed the findings and contributed to writing the manuscript.

Competing interests. We declare that no competing interests are present.

Acknowledgements. Parts of this study have been supported by the collaborative project GROCE2 (Greenland Ice Sheet Ocean Interaction) funded by the German Federal Ministry of Research and Education under the Grant No. 03F0855A. E.L. has been funded by the Helmholtz
350 Association Project AI-CORE 'Artificial Intelligence for COld REgions'. R.S. is supported by the German Research Foundation (DFG) under MU 1370/21-1. We want to thank Daniel Steinhage, the crew of Polar 5, Dean Emberly, Marc-André Verner, Luke Cirtwill, Ryan Schrader, the team of Villum Research Station and Station Nord for their support of the airborne campaign NG21.

References

Beyer, R. A., Alexandrov, O., and McMichael, S.: The Ames Stereo Pipeline: NASA's Open Source Software for Deriving and Processing Terrain Data, Earth and Space Science, 5, 537–548, https://doi.org/10.1029/2018EA000409, 2018.

Blatter, H.: Velocity and stress fields in grounded glaciers: a simple algorithm for including deviatoric stress gradients, Journal of Glaciology, 41, 333–344, https://doi.org/10.3189/S002214300001621X, 1995.

Borstad, C. P., Rignot, E., Mouginot, J., and Schodlok, M. P.: Creep deformation and buttressing capacity of damaged ice shelves: theory and application to Larsen C ice shelf, The Cryosphere, 7, 1931–1947, https://doi.org/10.5194/tc-7-1931-2013, 2013.

Braun, M., Humbert, A., and Moll, A.: Changes of Wilkins Ice Shelf over the past 15 years and inferences on its stability, The Cryosphere, 3, 41–56, https://doi.org/10.5194/tc-3-41-2009, 2009.

Christmann, J., Helm, V., Khan, S. A., Kleiner, T., Müller, R., Morlighem, M., Neckel, N., Rückamp, M., Steinhage, D., Zeising, O., and Humbert, A.: Elastic deformation plays a non-negligible role in Greenland's outlet glacier flow, Communications Earth & Environment, 2, https://doi.org/10.1038/s43247-021-00296-3, 2021.

Chudley, T. R., Christoffersen, P., Doyle, S. H., Bougamont, M., Schoonman, C. M., Hubbard, B., and James, M. R.: Supraglacial lake drainage at a fast-flowing Greenlandic outlet glacier, Proceedings of the National Academy of Sciences, 116, 25 468–25 477, https://doi.org/10.1073/pnas.1913685116, 2019.

Das, S. B., Joughin, I., Behn, M. D., Howat, I. M., King, M. A., Lizarralde, D., and Bhatia, M. P.: Fracture Propagation to the Base of the Greenland Ice Sheet During Supraglacial Lake Drainage, Science, 320, 778–781, https://doi.org/10.1126/science.1153360, 2008.

De Rydt, J., Reese, R., Paolo, F. S., and Gudmundsson, G. H.: Drivers of Pine Island Glacier speed-up between 1996 and 2016, The Cryosphere, 15, 113–132, https://doi.org/10.5194/tc-15-113-2021, 2021.

Doake, C. and Vaughan, D.: Rapid disintegration of the Wordie Ice Shelf in response to atmospheric warming, Nature, pp. 328–330, https://doi.org/10.1038/350328a0, 1991.

Glen, J. W.: The Creep of Polycrystalline Ice, Proceedings of the Royal Society of London. Series A, Mathematical and Physical Sciences, 228, 519–538, https://doi.org/10.1098/rspa.1955.0066, 1955.

Hale, R., Miller, H., Gogineni, S., Yan, J. B., Rodriguez-Morales, F., Leuschen, C., Paden, J., Li, J., Binder, T., Steinhage, D., Gehrmann, M., and Braaten, D.: Multi-channel ultra-wideband radar sounder and imager, in: 2016 IEEE International Geoscience and Remote Sensing Symposium (IGARSS), pp. 2112–2115, https://doi.org/10.1109/IGARSS.2016.7729545, 2016.

Hill, E. A., Carr, J. R., and Stokes, C. R.: A Review of Recent Changes in Major Marine-Terminating Outlet Glaciers in Northern Greenland, Frontiers in Earth Science, 4, https://doi.org/10.3389/feart.2016.00111, 2017.

Howat, I. M., Joughin, I., Fahnestock, M., Smith, B. E., and Scambos, T. A.: Synchronous retreat and acceleration of southeast Greenland outlet glaciers 2000–06: ice dynamics and coupling to climate, Journal of Glaciology, 54, 646–660, https://doi.org/10.3189/002214308786570908, 2008.

Howat, I. M., Negrete, A., and Smith, B. E.: The Greenland Ice Mapping Project (GIMP) land classification and surface elevation data sets, The Cryosphere, 8, 1509–1518, https://doi.org/10.5194/tc-8-1509-2014, 2014.

Humbert, A., Gross, D., Müller, R., Braun, M., van de Wal, R., van den Broeke, M., Vaughan, D., and van de Berg, W.: Deformation and failure of the ice bridge on the Wilkins Ice Shelf, Antarctica, Annals of Glaciology, 51, 49–55, https://doi.org/10.3189/172756410791392709, 2010.

Johnson, A., Hock, R., and Fahnestock, M.: Spatial variability and regional trends of Antarctic ice shelf surface melt duration over 1979–2020 derived from passive microwave data, Journal of Glaciology, 68, 533–546, https://doi.org/10.1017/jog.2021.112, 2022.

Joughin, I., Abdalati, W., and Fahnestock, M.: Large fluctuations in speed on Greenland's Jakobshavn Isbræ glacier, Nature, 432, 608–610, https://doi.org/10.1038/nature03130, 2004.

Joughin, I., Smith, B. E., Howat, I. M., Floricioiu, D., Alley, R. B., Truffer, M., and Fahnestock, M.: Seasonal to decadal scale variations in the surface velocity of Jakobshavn Isbrae, Greenland: Observation and model-based analysis, Journal of Geophysical Research: Earth Surface, 117, https://doi.org/10.1029/2011JF002110, 2012.

Joughin, I., Shean, D. E., Smith, B. E., and Floricioiu, D.: A decade of variability on Jakobshavn Isbræ: ocean temperatures pace speed through influence on mélange rigidity, The Cryosphere, 14, 211–227, https://doi.org/10.5194/tc-14-211-2020, 2020.

Joughin, I., Shapero, D., Smith, B., Dutrieux, P., and Barham, M.: Ice-shelf retreat drives recent Pine Island Glacier speedup, Science Advances, 7, eabg3080, https://doi.org/10.1126/sciadv.abg3080, 2021.

Khan, S. A., Kjær, K. H., Bevis, M., Bamber, J. L., Wahr, J., Kjeldsen, K. K., Bjørk, A. A., Korsgaard, N. J., Stearns, L. A., Van Den Broeke, M. R., et al.: Sustained mass loss of the northeast Greenland ice sheet triggered by regional warming, Nat. Clim. Change, 4, 292–299, 2014.

Khan, S. A., Bamber, J. L., Rignot, E., Helm, V., Aschwanden, A., Holland, D. M., van den Broeke, M., King, M., Noël, B., Truffer, M., Humbert, A., Colgan, W., Vijay, S., and Kuipers Munneke, P.: Greenland Mass Trends From Airborne and Satellite Altimetry During 2011-2020, Journal of Geophysical Research: Earth Surface, 127, e2021JF006 505, https://doi.org/10.1029/2021JF006505, 2022.

Krieger, L., Floricioiu, D., and Neckel, N.: Drainage basin delineation for outlet glaciers of Northeast Greenland based on Sentinel-1 ice velocities and TanDEM-X elevations, Remote Sensing of Environment, 237, 111 483, https://doi.org/10.1016/j.rse.2019.111483, 2020.

Larour, E., Seroussi, H., Morlighem, M., and Rignot, E.: Continental scale, high order, high spatial resolution, ice sheet modeling using the Ice Sheet System Model (ISSM), Journal of Geophysical Research, 117, F01 022, https://doi.org/10.1029/2011JF002140, 2012.

Libert, L., Wuite, J., and Nagler, T.: Automatic delineation of cracks with Sentinel-1 interferometry for monitoring ice shelf damage and calving, The Cryosphere, 16, 1523–1542, https://doi.org/10.5194/tc-16-1523-2022, 2022.

Lyard, F., Lefevre, F., Letellier, T., and Francis, O.: Modelling the global ocean tides: modern insights from FES2004, Ocean Dyn., 56, 394–415, https://doi.org/10.1007/s10236-006-0086-x, 2006.

Morlighem, M., Williams, C. N., Rignot, E., An, L., Arndt, J. E., Bamber, J. L., Catania, G., Chauché, N., Dowdeswell, J. A., Dorschel, B., Fenty, I., Hogan, K., Howat, I., Hubbard, A., Jakobsson, M., Jordan, T. M., Kjeldsen, K. K., Millan, R., Mayer, L., Mouginot, J., Noël, B. P. Y., O'Cofaigh, C., Palmer, S., Rysgaard, S., Seroussi, H., Siegert, M. J., Slabon, P., Straneo, F., van den Broeke, M. R., Weinrebe, W., Wood, M., and Zinglersen, K. B.: BedMachine v3: Complete bed topography and ocean bathymetry mapping of Greenland from multibeam echo sounding combined with mass conservation, Geophysical Research Letters, 44, 11 051–11 061, https://doi.org/10.1002/2017GL074954, 2017.

Mouginot, J., Rignot, E., Scheuchl, B., Fenty, I., Khazendar, A., Morlighem, M., Buzzi, A., and Paden, J.: Fast retreat of ZachariæIsstrøm, northeast Greenland, Science, 350, 1357–1361, https://doi.org/10.1126/science.aac7111, 2015.

Neckel, N., Franke, S., Helm, V., Drews, R., and Jansen, D.: Evidence of Cascading Subglacial Water Flow at Jutulstraumen Glacier (Antarctica) Derived From Sentinel-1 and ICESat-2 Measurements, Geophysical Research Letters, 48, e2021GL094 472, https://doi.org/10.1029/2021GL094472, e2021GL094472 2021GL094472, 2021.

Pattyn, F.: A new three-dimensional higher-order thermomechanical ice-sheet model: basic sensitivity, ice-stream development and ice flow across subglacial lakes, Journal of Geophysical Research, 108, 2382, https://doi.org/10.1029/2002JB002329, 2003.

Pavlis, N. K., Holmes, S. A., Kenyon, S. C., and Factor, J. K.: The development and evaluation of the Earth Gravitational Model 2008 (EGM2008), Journal of Geophysical Research: Solid Earth, 117, https://doi.org/10.1029/2011JB008916, 2012.

Rack, W. and Rott, H.: Pattern of retreat and disintegration of the Larsen B ice shelf, Antarctic Peninsula, Annals of Glaciology, 39, 505–510,
430   https://doi.org/10.3189/172756404781814005, 2004.

Rankl, M., Fürst, J. J., Humbert, A., and Braun, M. H.: Dynamic changes on the Wilkins Ice Shelf during the 2006–2009 retreat derived from satellite observations, The Cryosphere, 11, 1199–1211, https://doi.org/10.5194/tc-11-1199-2017, 2017.

Reeh, N., Mayer, C., Olesen, O. B., Christensen, E. L., and Thomsen, H. H.: Tidal movement of Nioghalvfjerdsfjorden glacier, northeast Greenland: observations and modelling, Ann. Glaciol., 31, 111–117, https://doi.org/10.3189/172756400781820408, 2000.

435   Rosenau, R., Scheinert, M., and Dietrich, R.: A processing system to monitor Greenland outlet glacier velocity variations at decadal and seasonal time scales utilizing the Landsat imagery, Remote Sensing of Environment, 169, 1–19, https://doi.org/10.1016/j.rse.2015.07.012, 2015.

Rückamp, M., Neckel, N., Berger, S., Humbert, A., and Helm, V.: Calving Induced Speedup of Petermann Glacier, Journal of Geophysical Research: Earth Surface, 124, 216–228, https://doi.org/10.1029/2018JF004775, 2019.

440   Scambos, T. A., Hulbe, C., Fahnestock, M., and Bohlander, J.: The link between climate warming and break-up of ice shelves in the Antarctic Peninsula, Journal of Glaciology, 46, 516–530, https://doi.org/10.3189/172756500781833043, 2000.

Schaffer, J., Kanzow, T., von Appen, W.-J., von Albedyll, L., Arndt, J. E., and Roberts, D. H.: Bathymetry constrains ocean heat supply to Greenland's largest glacier tongue, Nat. Geosci., 13, 227–231, https://doi.org/10.1038/s41561-019-0529-x, 2020.

Shepherd, A., Ivins, E., Rignot, E., Smith, B., van den Broeke, M., Velicogna, I., Whitehouse, P., Briggs, K., Joughin, I., Krinner, G., Nowicki,
445   S., Payne, T., Scambos, T., Schlegel, N., A, G., Agosta, C., Ahlstrøm, A., Babonis, G., Barletta, V. R., Bjørk, A. A., Blazquez, A., Bonin, J., Colgan, W., Csatho, B., Cullather, R., Engdahl, M. E., Felikson, D., Fettweis, X., Forsberg, R., Hogg, A. E., Gallee, H., Gardner, A., Gilbert, L., Gourmelen, N., Groh, A., Gunter, B., Hanna, E., Harig, C., Helm, V., Horvath, A., Horwath, M., Khan, S., Kjeldsen, K. K., Konrad, H., Langen, P. L., Lecavalier, B., Loomis, B., Luthcke, S., McMillan, M., Melini, D., Mernild, S., Mohajerani, Y., Moore, P., Mottram, R., Mouginot, J., Moyano, G., Muir, A., Nagler, T., Nield, G., Nilsson, J., Noël, B., Otosaka, I., Pattle, M. E., Peltier, W. R., Pie,
450   N., Rietbroek, R., Rott, H., Sandberg Sørensen, L., Sasgen, I., Save, H., Scheuchl, B., Schrama, E., Schröder, L., Seo, K.-W., Simonsen, S. B., Slater, T., Spada, G., Sutterley, T., Talpe, M., Tarasov, L., van de Berg, W. J., van der Wal, W., van Wessem, M., Vishwakarma, B. D., Wiese, D., Wilton, D., Wagner, T., Wouters, B., Wuite, J., and Team, T. I.: Mass balance of the Greenland Ice Sheet from 1992 to 2018, Nature, 579, 233–239, https://doi.org/10.1038/s41586-019-1855-2, 2020.

Steinemann, S.: Results of Preliminary Experiments on the Plasticity of Ice Crystals, Journal of Glaciology, 2, 404–416,
455   https://doi.org/10.3189/002214354793702533, 1954.

Wessel, B., Bertram, A., Gruber, A., Bemm, S., and Dech, S.: A new high-resolution elevation model of Greenland derived from TanDEM-X, in: XXIII ISPRS Congress, vol. III-7, pp. 9–16, https://doi.org/10.5194/isprsannals-III-7-9-2016, 2016.

Wilson, N. and Straneo, F.: Water exchange between the continental shelf and the cavity beneath Nioghalvfjerdsbræ (79 North Glacier), Geophys. Res. Lett., 42, 7648–7654, https://doi.org/10.1002/2015GL064944, 2015.

460   Zhang, Q., Huai, B., van den Broeke, M. R., Cappelen, J., Ding, M., Wang, Y., and Sun, W.: Temporal and Spatial Variability in Contemporary Greenland Warming (1958–2020), Journal of Climate, 35, 2755–2767, https://doi.org/10.1175/JCLI-D-21-0313.1, 2022.